




# Design, synthesis, and biological evaluation of a small molecule oral agonist of the glucagon-like-peptide-1 receptor

Received for publication, December 22, 2021, and in revised form, March 15, 2022. Published, Papers in Press, April 2, 2022.

<https://doi.org/10.1016/j.jbc.2022.101889>

Khyati Girdhar<sup>1</sup>, Shilpa Thakur<sup>1</sup> , Pankaj Gaur<sup>1,†</sup> , Abhinav Choubey<sup>1,‡</sup>, Surbhi Dogra<sup>1</sup>, Budheswar Dehury<sup>2</sup> , Sunil Kumar<sup>3</sup>, Bidisha Biswas<sup>1</sup>, Durgesh Kumar Dwivedi<sup>4</sup>, Subrata Ghosh<sup>1</sup>, and Prosenjit Mondal<sup>1,\*</sup>

From the <sup>1</sup>School of Basic Sciences, Indian Institute of Technology Mandi, Mandi, HP, India; <sup>2</sup>Bioinformatics Division, ICMR-Regional Medical Research Centre, Bhubaneswar, India; <sup>3</sup>ICAR-Indian Agricultural Statistics Research Institute (IASRI), PUSA, New Delhi, India; <sup>4</sup>Pharmacology Division, CCRAS-Regional Ayurveda Research Institute, Gwalior, MP, India

Edited by Qi-Qun Tang

An absolute or relative deficiency of pancreatic  $\beta$ -cells mass and functionality is a crucial pathological feature common to type 1 diabetes mellitus and type 2 diabetes mellitus. Glucagon-like-peptide-1 receptor (GLP1R) agonists have been the focus of considerable research attention for their ability to protect  $\beta$ -cell mass and augment insulin secretion with no risk of hypoglycemia. Presently commercially available GLP1R agonists are peptides that limit their use due to cost, stability, and mode of administration. To address this drawback, strategically designed distinct sets of small molecules were docked on GLP1R ectodomain and compared with previously known small molecule GLP1R agonists. One of the small molecule PK2 (6-((1-(4-nitrobenzyl)-1H-1,2,3-triazol-4-yl)methyl)-6H-indolo[2,3-b]quinoxaline) displays stable binding with GLP1R ectodomain and induces GLP1R internalization and increasing cAMP levels. PK2 also increases insulin secretion in the INS-1 cells. The oral administration of PK2 protects against diabetes induced by multiple low-dose streptozotocin administration by lowering high blood glucose levels. Similar to GLP1R peptidic agonists, treatment of PK2 induces  $\beta$ -cell replication and attenuate  $\beta$ -cell apoptosis in STZ-treated mice. Mechanistically, this protection was associated with decreased thioredoxin-interacting protein expression, a potent inducer of diabetic  $\beta$ -cell apoptosis and dysfunction. Together, this report describes a small molecule, PK2, as an orally active non-peptidic GLP1R agonist that has efficacy to preserve or restore functional  $\beta$ -cell mass.

The global burden of diabetes has expanded considerably over the past few decades, affecting approximately 425 million individuals in 2017 and over a million youngsters and teenagers (1). As the incidence of diabetes increases at an alarming rate, it is becoming imperative to shift the research focus that can lead to new therapies for preventing or delaying the onset of disease. Among all therapeutics available for the treatment of diabetes, glucagon-like-peptide-1 receptor (GLP1R) agonists

have an advantage in protecting  $\beta$ -cell mass, augmenting glucose-dependent insulin secretion with low hypoglycemic risk (2). GLP1R is a member of the class B1 (secretin-like receptors) family of G-protein coupled receptors, which spanned seven transmembrane domains. GLP-1 binding to the receptor stimulates multiple signaling pathways. One of the pathways that ensure  $\beta$ -cell mass and insulin secretion is the activation of  $G_{\alpha s}$  that activates membrane-associated adenylyl cyclases. Adenylyl cyclase activation increases intracellular cAMP. An increase in cAMP activates PKA that phosphorylates Ser133 of cAMP response element-binding protein (CREB), inducing  $\beta$ -cell proliferation (3). Repeated and prolonged GLP1R stimulation through phosphorylation of specific residues at the C-terminal by its ligand also results in receptor internalization (4).

Exenatide, liraglutide, and other long-acting analogs of GLP-1 are accessible therapeutics for diabetes mellitus (5). However, there are several disadvantages associated with their route of administration, high cost, and instability due to their peptide nature. To overcome these limitations of peptide agonists of GLP1R, many small molecule GLP1R agonists like 2-(2-methyl)thiadiazolylsulfanyl-3-(trifluoromethyl)-6,7-dichloroquinoxaline (compound 1), 6,7-dichloro-2-methylsulfonyl-3-N-tert-butylaminoquinoxaline (compound 2) (6), pyrimidine, 4-(3,4-dichlorophenyl)-2-(ethylsulfonyl)-6-(trifluoromethyl) (compound A), 4-(3-benzyloxyphenyl)-2-ethylsulfinyl-6-(trifluoromethyl) pyrimidine (7), (S)-2-cyclopentyl-N-((1-isopropylpyrrolidin-2-yl)-9-methyl-1-oxo-2,9-dihydro-1H-pyrido[3,4-b]indole-4-carboxamide ((S)-8) (8), substituted cyclobutanes (1,3-bis[[4-(tert-butoxy-carbonylamino) benzoyl]amino]-2,4-bis[3-methoxy-4-(thiophene-2-carboxyloxy)-phenyl]cyclobutane-1,3-dicarboxylic acid) (Boc-5), and S4P, azoanthracenes (TTPxxx), thiophenes, phenylalanines, flavonoids has been introduced from last 20 years but none of these have been approved for therapeutic use until last year. Oral semaglutide, first non-injectable formulation of a GLP-1 receptor agonist approved by the U.S. Food and Drug Administration (9). This connotes the requirement for a new small molecule agonist of GLP1R. GLP1R has an independently folded globular ectodomain (ECD) at their N-termini; any peptide agonist initiates

<sup>†</sup> These authors contributed equally to this work.

\* For correspondence: Prosenjit Mondal, [prosenjit@iitmandi.ac.in](mailto:prosenjit@iitmandi.ac.in).

## Small molecule agonist of glucagon-like-peptide-1 receptor

receptor signaling by binding to the transmembrane domain and several amino acid residues on the ECD (10). Considering the importance of amino acid residues present on ECD in ligand binding, GLP1R agonist small molecules interaction and their dynamics with the extracellular domain of the GLP1R has been investigated (11). In this article, we designed a *de novo* series of a small molecule by considering the role of hydrophobic interactions (mainly  $\pi$ - $\pi$  stacking) in ligand binding with the GLP1R extracellular domain.

This report presents 6-((1-(4-nitrobenzyl)-1H-1,2,3-triazol-4-yl)methyl)-6H-indolo[2,3-b]quinoxaline (PK2), a small molecule GLP1R agonist that protects  $\beta$ -cell mass by decreasing  $\beta$ -cell apoptosis and increasing  $\beta$ -cell proliferation.

### Results

#### Lead series optimization: molecular docking to screen small molecule agonist of GLP1R

The crystal structure of the ECD of GLP1R (Fig. 1A) (12) and its interaction with its allosteric agonists have revealed an exciting opportunity for structure-based drug design. In search of a new GLP1R agonist, we screened structurally modified small molecules on ECD of GLP1R using AutoDock software (13). The GLP1R–small molecule complexes were ranked according to their binding affinity (Table S1). The structure of selected three molecules (PK2, PK3, and PK4) out of 96 screened based on high-binding affinity and Lipinski rule are shown in (Fig. 1B). The binding modes of the lowest binding conformer of three molecules were analyzed using the discovery studio visualizer (DSV) (Fig. 1C).

PK2, PK3, and PK4 exhibit almost comparable binding modes and interactions with the ECD of GLP1R. These compounds develop  $\pi$ - $\pi$  stacking with the residue Trp42, TRP87, Trp39, and Trp69. PK2 and PK4 show some conventional H-bond with the Glu45 and Arg40, Arg43 respectively, while PK3 displays no H-bond formations. The binding affinity and the binding modes of PK2, PK3, and PK4 indicate the lowest binding affinity than the reported allosteric agonist along with similar binding sites. These results define the

interactions of the compounds with the ECD of GLP1R. By considering binding energy and  $\pi$ - $\pi$  interactions as the essential parameters for the stability of receptor–molecule interaction, we synthesized three molecules based on these parameters and the Lipinski rule of five for further analysis. The steps involved in the reactions are portrayed schematically in Fig. 2

#### Internalization of GLP1R and its signaling axis: lead molecule in-vitro screening

Repeated activation of GLP1R *via* its ligand causes receptor desensitization or internalization. To determine the efficacy of synthesized compound with GLP1R, spark-GFP tagged human GLP1R plasmid (hGLP1R-GFP) was transfected in human liver carcinoma HepG2 cells. Cells were stimulated with 50  $\mu$ M of each compound (PK2-PK4), Ex-4 (20 nM) was used as a positive control, and DMSO as a vehicle for 1 h. Confocal microscopy images revealed that compounds PK2, PK3, and PK4 rapidly internalized GLP1R receptors (Fig. 3A).

For further *in vitro* and *in vivo* studies, we used PK2, considering the highest solubility of PK2 (10 mg/ml in DMSO) and have zero violation as drug-likeness (follow Lipinski, Veber, Ghose, Egan, Muegge rules) than PK3 and PK4. Additionally, we also determined PK2 binding for GLP1R in the presence of the GLP1R competitive antagonist, Exendin-9 (Ex-9). hGLP1R-transfected HepG2 cells were treated with Ex-9 (300 nM) and Ex-9 along with PK2. We observed Ex-9 was blocking PK2-mediated GLP1R internalization (Fig. 3B) as well as extracellular regulated kinase phosphorylation (14)(Fig. S4, A and B). These findings demonstrate PK2 binding on hGLP1R.

Next, we determined the agonist activity of PK2 by measuring the cAMP levels using hGLP1R-transfected 293A human embryonic kidney cells. PK2 increases intracellular cAMP level with an increase in concentration with a half-maximal effective concentration (EC<sub>50</sub>) of 43.66 nM (Fig. 3C). Moreover, we also determined the PK2 effect on GLP1R signaling by examining PKA activity and CREB

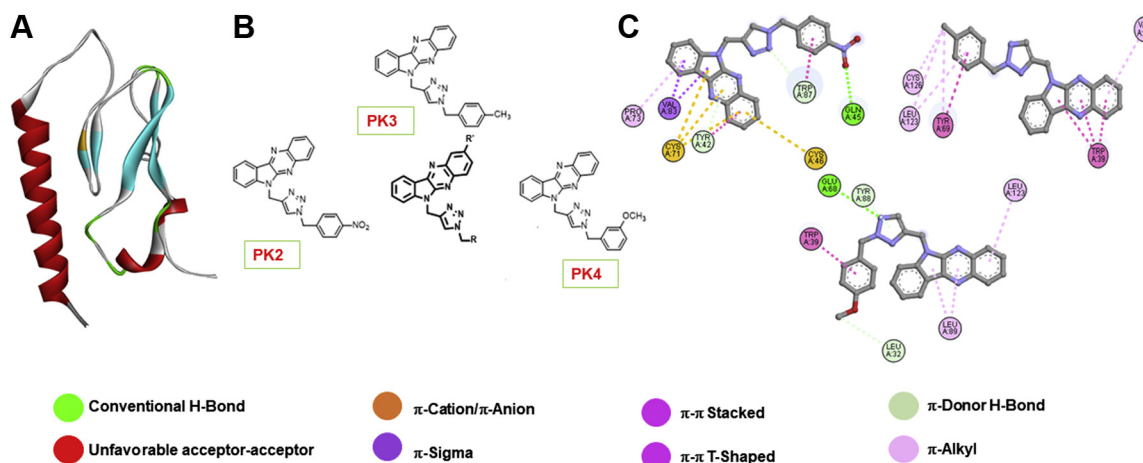


**Figure 1. Molecular docking of small molecule library.** A, structure of ECD of GLP1R PDB: [3ioj]. B, chemical structure of selected small molecule library. C, confine representation of the binding site of selected small molecule library. ECD, ectodomain; GLP1R, glucagon-like-peptide-1 receptor.

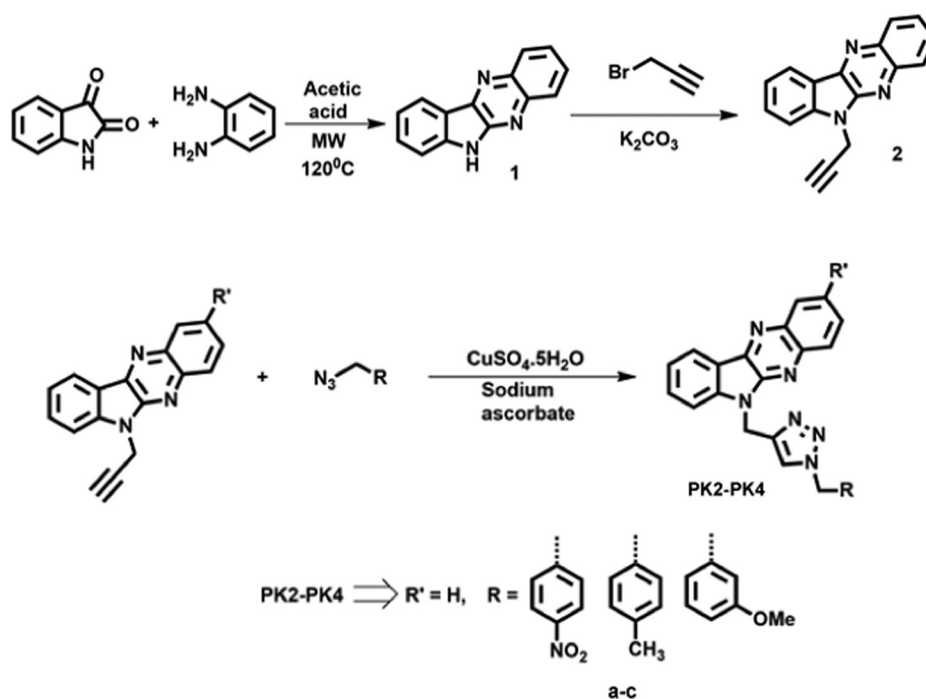


Figure 2. Synthesis Strategy of small molecule library and route for analog synthesis.

phosphorylation. PKA activity was determined utilizing the immortalized PKA substrate-bound ELISA kit. While PK2 was treated on hGLP1R transfected 293A cells, PKA activity was measured using ELISA. The results suggest (Fig. S4C) an increment of 1.6 fold in PKA activity on treatment with PK2. Furthermore, Western blot analysis showed PK2 (50  $\mu$ M) increases CREB phosphorylation at Ser133 by 1.7 fold (Fig. S4, D and E). These results suggest that PK2 binds and activates GLP1R downstream signaling by activating PKA activity and inducing CREB phosphorylation. These findings demonstrate the agonistic activity of PK2 for hGLP1R.

Next, to determine the biological activity of PK2 *in vitro*, we used INS-1 cells, the rat  $\beta$ -cells that respond to insulin secretion in physiological glucose concentration. PK2 shows a 1.45-fold increase in insulin secretion in the presence of high glucose concentration (16.7 mM) (Fig. 3D). Thus, this result represents that PK2 not only presents agonism but also shows its activity by increasing insulin secretion in INS-1 cells.

#### Dynamic stability of GLP1R–PK2 complex

Next, for better sampling and to gauge the accuracy of docked conformation, multiple molecular dynamics (MD) simulations of the GLP1R–PK2 complex were conducted for 100 ns. The conformations obtained during the 100 ns simulation of the three systems were analyzed in detail, and the RMSD, Rg, and C $\alpha$ -root mean square fluctuations (RMSF) were calculated to determine the average change in displacement of a selection of atoms for a particular frame to the initial reference frame. The RMSD plots for the PK2–GLP1R complex obtained are displayed (Fig. 4A), and close inspection indicates the RMSD of the complex is maintained below  $\sim$ 4 Å. The black, red, and green lines indicate RMSD three seeds during 100 ns, where the RMSD is in the range of 2 to 3 Å,

which suggests the stable nature of the three complexes. The Rg is used to determine the concretion of the system. Like, RMSD, the trend of gyradius (Fig. 4B) suggests that the Rg value of the PK2 complex is in the range of 14 to 15 Å, which indicates the PK2–GLP1–R complex is highly compact during the simulation process. RMSF value, which determines the conformation change in the individual residue of the protein after ligand binding, is calculated based on the C $\alpha$  of each amino-acid residue of GLP1R. The N-terminal, C-terminal, and the amino acid residues present at the loop/turn display high flexibility in the RMSF profile (Fig. 4C). The high peak RMSF in some of the specific regions of GLP1R–PK2 systems may be due to the flexibilities of these residues toward PK2. The fundamental stability of a complex is recognized by intermolecular H-bonds. The PK2 interacts with the extracellular domain of the GLP1R with an average of 3 to 4 H-bonds, as evidenced from intermolecular analysis over 100 ns trajectories (Fig. 4, D–F). Further, the clustering algorithm with an RMSD cut-off of 2.0 Å was employed to determine the conformational heterogeneity in the GLP1R–PK2 complex. Analysis of all the top-ranked cluster complexes displayed prominent hydrophobic interactions (mostly  $\pi$ – $\pi$  stacking and  $\pi$ -alkyl interaction) along with some of the conventional H-bonds (as summarized in Table S2).

Next, to find the most prominent motions of functional protein, essential dynamics were used. The movement of the main-chain atoms of the extracellular domain of GLP1R was obtained from the eigenvalues (Fig. 4G), which are gained by diagonalizing the matrix against eigenvector indices. To further probe the conformational changes upon ligand binding, we projected the movement of backbone atoms to phase space utilizing PC1 and PC2, which displayed all the systems occupied in the least conformational space (Fig. 4H). To visualize the



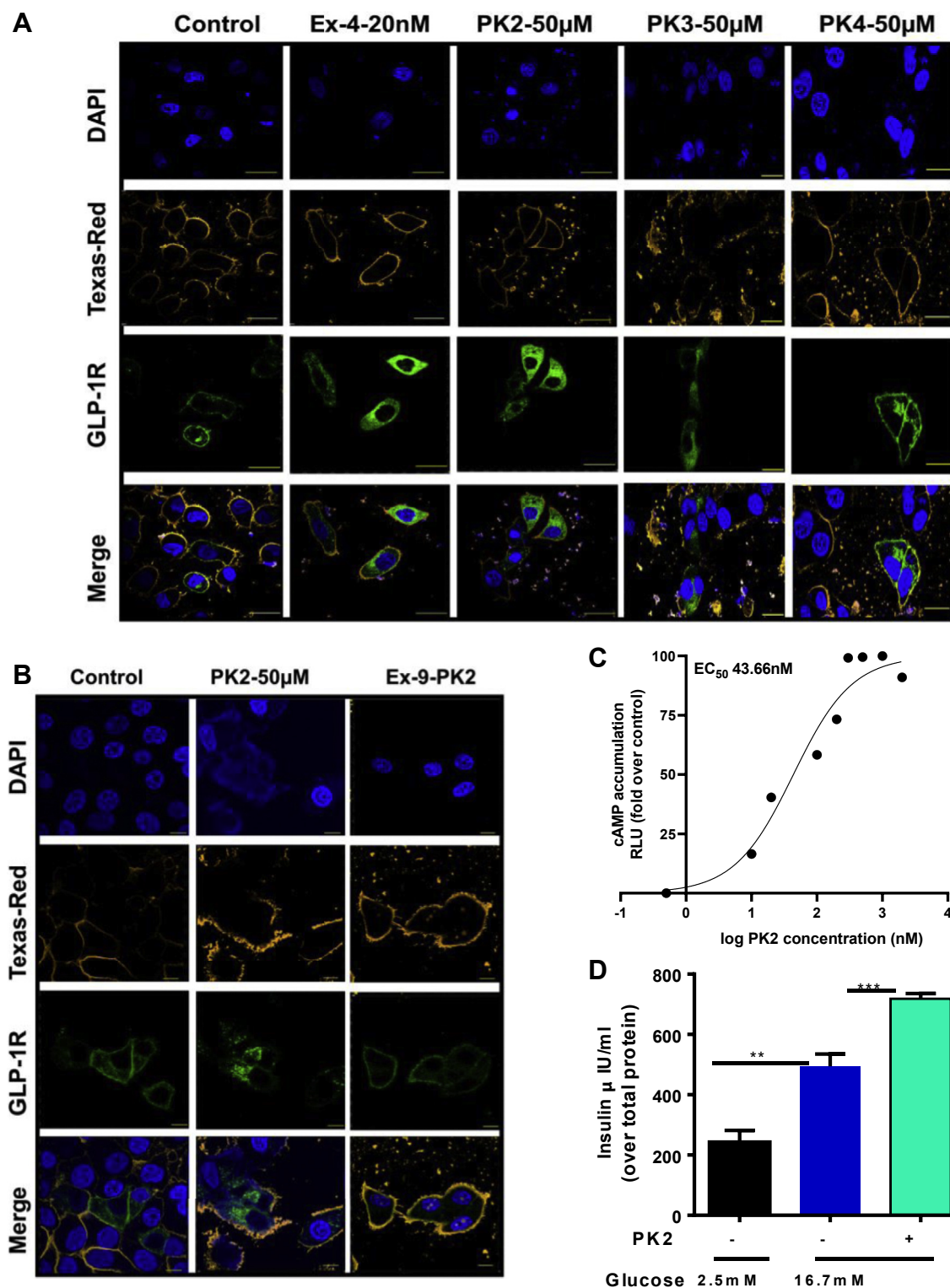


**Figure 3. Validation of the binding of a small molecule with GLP1R.** A, HepG2 cells were treated with each compound of PK2-PK4 (50  $\mu$ M) for 1 h, Ex-4 (20 nM) as positive control, and DMSO as vehicle. The scale bars represent 20  $\mu$ m. B, HepG2 cells were treated with 300 nM of Ex-9 for 15 min and stimulated with PK2-50  $\mu$ M for 1 h, and the cells were analyzed under confocal microscope. The scale bars represent 20  $\mu$ m. C, cAMP level in hGLP1R transfected 293A cells at different PK2 concentration (0.5, 10, 20, 100, 200, 300, 500, 1000, and 2000 nM) for after 4 h treatment, where control cells treated with DMSO as vehicle (n = 3)/group. EC<sub>50</sub> was calculated using Graphpad prism. D, insulin secretion in INS-1 cells at different glucose concentrations (2.5 mM and 16.7 mM). PK2 was treated in the presence of high glucose (16.7 mM) (n = 3/group). Data expressed mean  $\pm$  SEM of triplicates, \*\*p < 0.01, \*\*\*p < 0.001 of control (DMSO). GLP1R, glucagon-like-peptide-1 receptor.

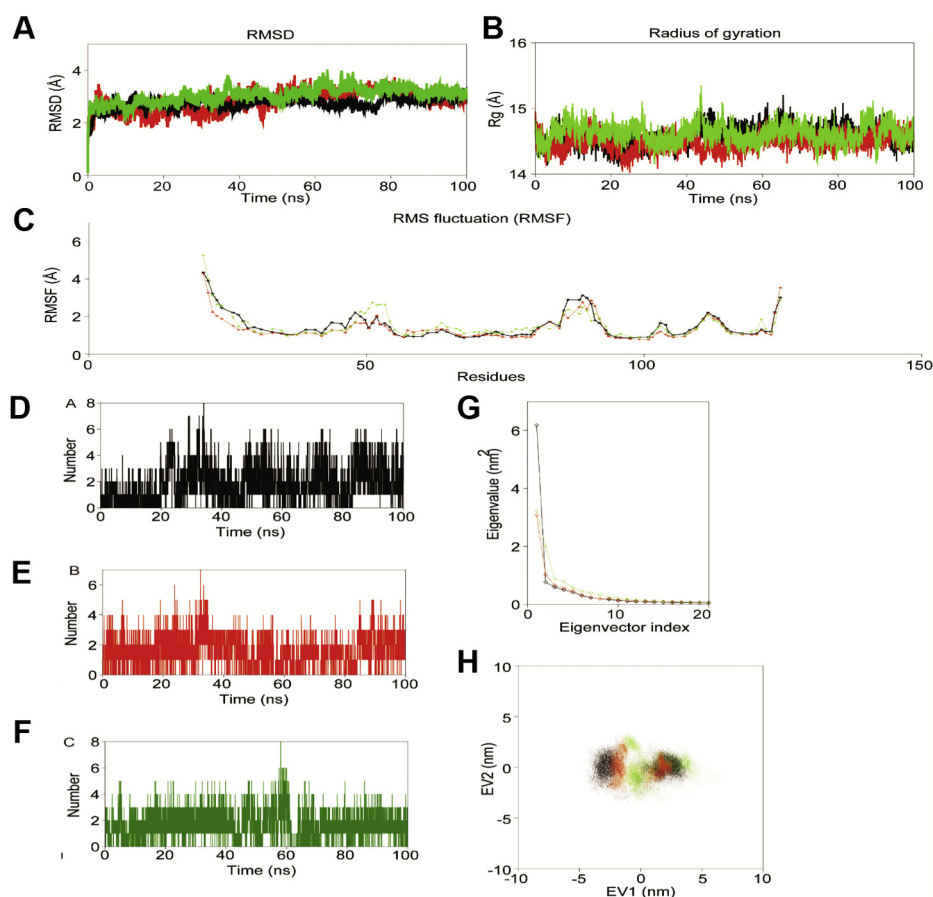


**Figure 4. Dynamics stability of GLP1R-PK2 complexes over 100 ns MD simulation in aqueous solution.** A, RMSD profile with respect to time of backbone atoms of complexes during 100 ns MD simulations. B, conformational analysis of complexes displaying the radius of gyration over 100 ns MD simulations. C, the  $\alpha$ -RMSF profile of complexes during MD simulation. D, E, and F, analysis of variation of intermolecular H-bonds of GLP1R-PK2 during 100 ns MD simulation. G, PCA displaying the eigenvalues versus eigenvector indices obtained from the main-chain atoms covariance matrix. H, the 2D projection of GLP1R-PK2 complex over in phase space along the first two principal eigenvectors (EV1 and EV2) components during three seeds of 100 ns MD (Black: Simulation 1, red: Simulation 2, and green: Simulation 3). GLP1R, glucagon-like-peptide-1 receptor; PCA, principal component analysis; RMSF, root mean square fluctuations.

movements graphically, porcupine plots were constructed using the mode vectors.py script, which revealed that most of the motions are due to terminal end residues and loops/turns connecting adjacent  $\beta$ -strands of GLP1-R (Fig. S2B). To envisage the energy minima of the landscape of GLP1-R systems from the three independent MD simulations, we calculated the FEL against the first two principal components, PC1 and PC2 (Fig. S3A). The size and shape of the minimal energy area reveal the stability of the three complexes where FEL of simulations 1 and 3 displayed the same shape while simulation 2 showed a somewhat small and compact shape which perfectly corroborates with the findings of principal component analysis. Overall, for the three independent simulations, we observed a single centralized and concentrated energy profile for GLP1R-PK2 systems, indicating the least structural changes in all the systems.

To further probe the binding-free energy of the GLP1R-PK2 complex system, the molecular mechanics-based Poisson-Boltzmann surface area (MM/PBSA) method was used. The binding-free energy of the three complexes was computed to be -36.01, -27.08, and -10.81 kJ/mol<sup>-1</sup>. As evident from intermolecular contact analysis, simulation 3 displayed the least

number of nonbonded contacts, which can be attributed to the lower free energy of the system. Overall binding-free energy analysis displayed that nonpolar solvation energy ominously contributes to the total binding energy. The post-MD intermolecular contact analysis revealed that the electrostatic and van der Waals interactions dominate among the nonbonded contacts.

Further, comparative intermolecular contact analysis of pre- and post-MD uncovered the critical amino acid residues that have the most severe impact on the stability of the GLP1R-PK2 complex (Table S2). Simulation 1 displayed more or less the same contact plots with intended amino acids throughout MD. Therefore, we speculate that the mode of binding of PK2 with GLP1R is the most probable mode of binding and illustrated in Fig. S3, C and D). As evident from Table S2, Val30, Trp87, and Gln45 formed crucial H-bonds with PK2, while Tyr42 formed many  $\pi$ - $\pi$  stacking contacts indicating their vital role in ligand recognition.

#### PK2 pharmacokinetics and tissue distribution study in mice

*In silico* and *in vitro* observations indicate PK2 is a stable GLP1R agonist. To further analyze the PK2 activity in the

mouse model of diabetes, we first determine PK2 distribution and pharmacokinetics *in vivo* (15). Safe and effective dose of PK2 (25 mg/kg) was selected based on dose-dependent study (0.1, 1, 10, 25, 50 mg/kg body weight) in BALB/c mice. Furthermore, no abnormal behavior or acute toxicity was observed in animals in the selected dose in 30 days of treatment. The *in vivo* pharmacokinetic study in BALB/c mice demonstrates the mean plasma concentration *versus* time profiles of PK2 on an oral administration of a single dose of 25 mg/kg body weight (Fig. 5A). The value of pharmacokinetics parameters is shown in Table 1. The results indicate that PK2 resulted in fast absorption from the gastrointestinal tract, rapidly reaching  $t_{max}$  in 1 h. PK2 shows a higher volume of distribution ( $V_D$ ) at a steady state of 38.88 l, which shows PK2 ability to bind with the tissue and plasma protein. PK2 exhibited a plasma half-life of 4.8 h ( $t_{1/2}$ ) and 7.79 l/hr of plasma clearance ( $C_L$ ), indicating rapid absorption with a normal clearance rate. Tissue distribution results of PK2 in mice after 2 h of oral administration indicate that PK2 was distributed highly among the liver, kidney, and pancreas with no traces in the heart, lungs, and spleen. A small amount of PK2 was detectable in the brain, which indicates that the PK2 can cross the blood-brain barrier (Fig. 5B).

## Oral administration of PK2 protects against STZ-induced pancreatic $\beta$ -cell apoptosis and dysfunction

$\beta$ -cell death or dysfunction plays a critical role in the pathophysiological progression of type 1 diabetes mellitus (T1DM) and type 2 diabetes mellitus (T2DM) (16). To further analyze the protective and reversal effect of PK2 on pancreatic  $\beta$ -cells *in vivo*, we screened the potential role of PK2 against the STZ-induced diabetic mouse model; a scheme designed presented in Figure 6A. Mice were divided into four groups (control; oral gavage with CMC suspension, STZ; oral gavage with CMC suspension and provided with multiple-dose of STZ, pre-PK2; oral gavage with PK2 in CMC suspension 3 days before multiple doses of STZ, post-PK2; oral gavage with PK2 in CMC suspension 1 day after a single dose of STZ). Blood glucose was measured from the tail vein every alternate day, and body weight was measured on random days until mice were sacrificed (a total of 18 days). Mice treated with PK2 and STZ both show increased body weight compared to STZ only (Fig. 6B). PK2 reduces the plasma glucose levels by 1.4-

**Table 1**

Table representing pharmacokinetics parameters

S.No.	Parameters	Values
1	K(Eliminatory rate constant)	0.2003 h <sup>-1</sup>
2	Area of last	320.1451 ng h/ml
3	AUC (0- t)	3210.272 ng h/ml
4	AUMC (0-t)	13,601.58 ng h/ml
5	AUMC (0- $\infty$ )	4120.97 ng h/ml
6	Dose	25 mg/Kg
7	$V_D$ (Apparent volume of distribution)	38.882 l
8	$C_L$ (Clearance)	7.7875 l/h
9	$t_{1/2}$ (Elimination half life)	4.8565 h
10	$C_{max}$	787.217 ng/ml
11	$t_{max}$	1 h

fold in both the groups (pre-PK2 and post-PK2) compared to STZ only (Fig. 6C). To further explore the reason for reduced blood glucose levels, serum insulin levels were measured from all experimental groups at the end of the study. There is a 7-fold reduction in the serum insulin levels in the STZ group. Nevertheless, PK2-treated groups recover serum insulin levels up to 6-fold (Fig. 6D).

Weigh of the pancreas at the termination of the study revealed protection in pancreas weight in PK2 groups (Fig. S5A). To examine increased islets mass caused in the PK2 groups, we performed H&E on the pancreatic sections. The staining of pancreatic sections showed significantly bigger islets area in mice of both pre-PK2 and post-PK2 groups than in the STZ mice group. PK2 appears to protect mice from STZ-induced damage to islets mass (Fig. S5B). This data implies there is a conservation of islets area in mice treated with PK2.

Next, to determine the protection of  $\beta$ -cell mass between these groups, we performed immunohistochemistry on the pancreatic section using insulin antibodies. Interestingly, there was the preservation of 4-fold in  $\beta$ -cell mass in both pre-PK2 and post-PK2 groups compared to STZ (Fig. 6, E–G). Next, determining the protection of  $\beta$ -cell mass by PK2 is either due to inhibition of apoptosis or increased proliferation. We performed TUNEL and Ki67 staining on the pancreata sections. TUNEL assay was performed to determine the apoptotic  $\beta$ -cell in the pancreatic islets. Figure 7, A and B represents a reduction of the 3-fold number of TUNEL-positive cells in both PK2 groups in the pancreatic islets compared to the STZ group.

Proliferating  $\beta$ -cells were identified by nuclear colocalization of proliferation marker Ki67 in the nucleus of insulin-positive islet cells (Fig. 7C). The results showed a significant

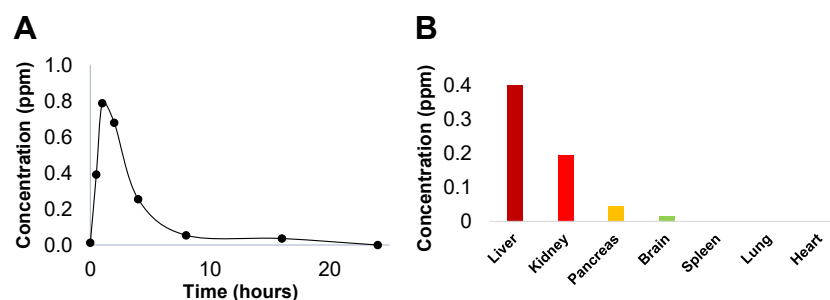


**Figure 5. Pharmacokinetics and tissue distribution study of PK2.** A, PK2 concentration was measured in blood plasma after oral administration at 25 mg/kg PK2 at different time points. B, PK2 concentrations were measured in various organs (Pancreas, Heart, Brain, Lung, Spleen, Kidney, and Liver) after 2 h of oral administration.



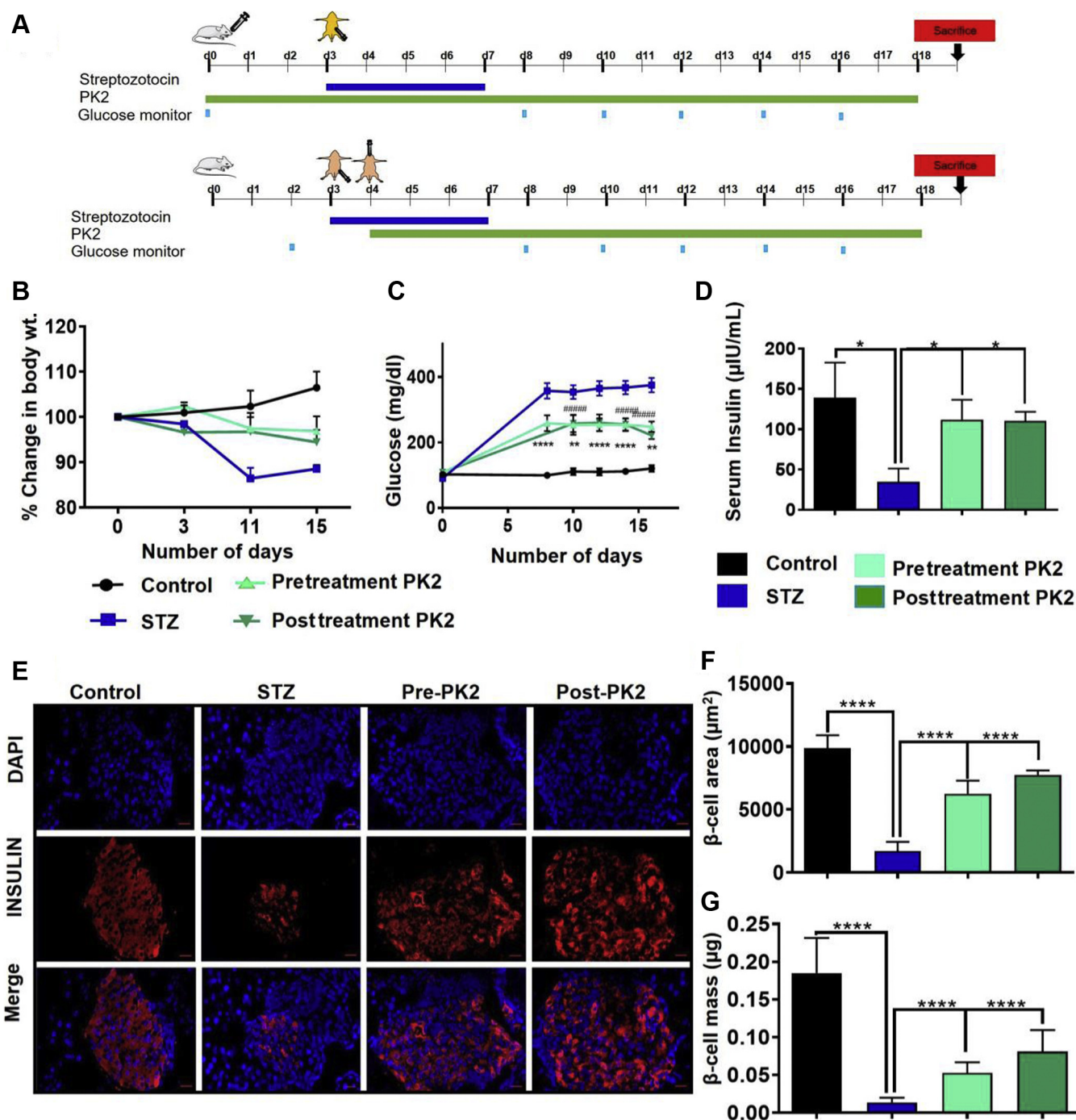


**Figure 6. PK2 effect on STZ treatment.** A, schematic diagram of the treatment strategy. B, bodyweight in control, STZ, pre-PK2, and post-PK2 groups. C, plasma glucose levels after 5 days of STZ treatment in mice groups,  $**p < 0.05$ ,  $****p < 0.001$  of STZ pre-PK2,  $#####p < 0.001$  of STZ, post-PK2. D, serum insulin level of all mice groups. Data expressed mean  $\pm$  SEM of triplicates,  $*p < 0.05$ . E, representative immunofluorescence images of the pancreatic tissue sections. The scale bars represent 20  $\mu$ m. F and G,  $\beta$ -cell morphometric analysis. Graphical representation of the indicated parameters of  $n \geq 5$  in each group, mean  $\pm$  SEM; (F and G)  $****p < 0.0001$ .

proliferation ( $p = 0.04$ ,  $*p < 0.05$ ) in the STZ group's islets compared to control islets. Moreover, PK2 showed a 1.7-fold more prominent effect in the enhancement of  $\beta$ -cell proliferation (Fig. 7, C and D). Overall, these results confirm that PK2 can protect pancreatic  $\beta$ -cell apoptosis and dysfunction induced by STZ *in vivo*. PK2 mainly conferred its  $\beta$ -cell protecting effect by attenuating  $\beta$ -cell apoptosis and inducing  $\beta$ -

cell proliferation thus, in turn, increases the  $\beta$ -cell mass and thereby conferring improved glycemic control.

#### PK2 inhibits TXNIP expression in $\beta$ -cells

TXNIP is a potent inducer of diabetic  $\beta$ -cell apoptosis and dysfunction, and inhibition of TXNIP prevents diabetes in mouse models of T1DM and T2DM (17, 18). We determined

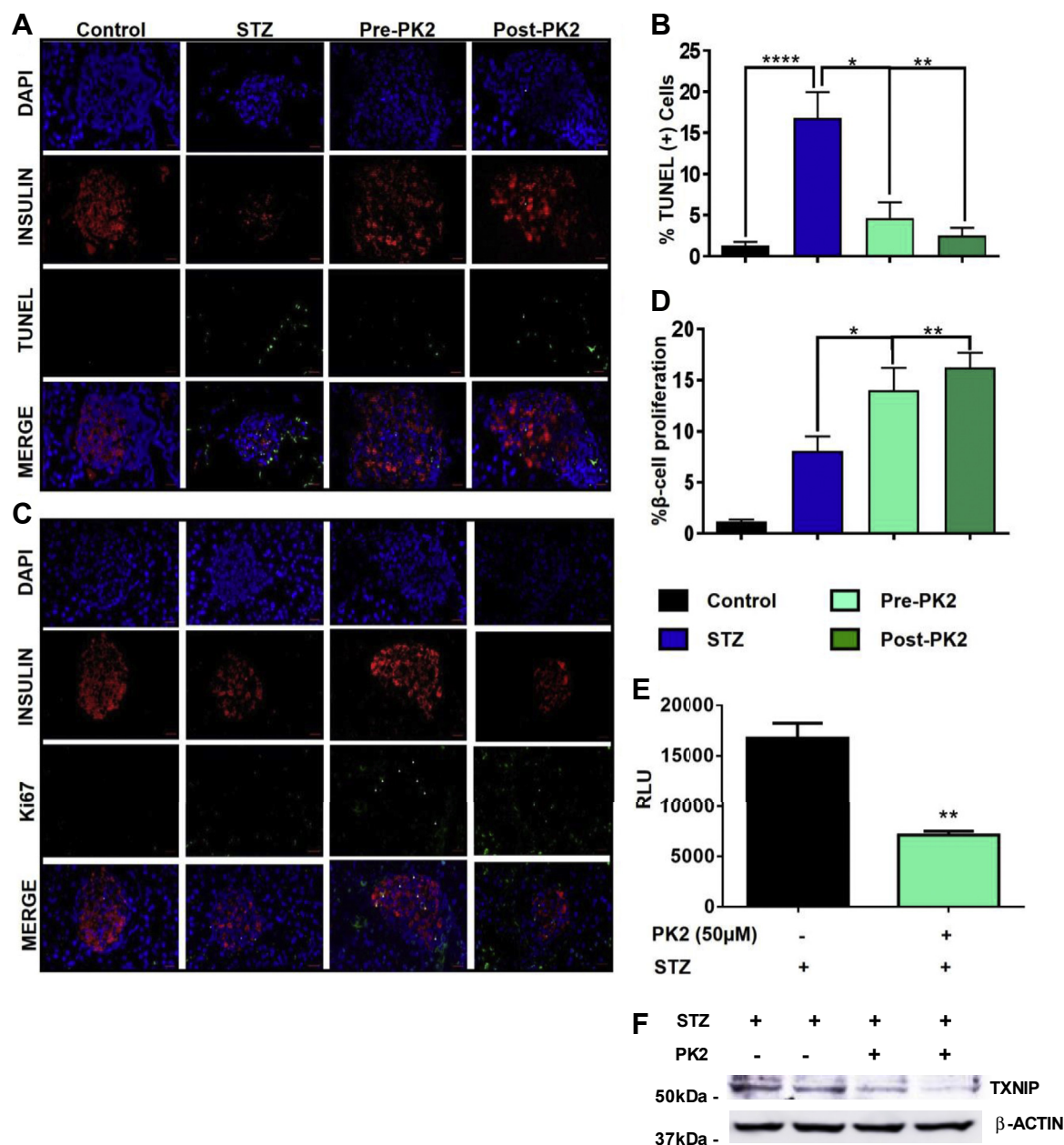


**Figure 7. PK2 effect on β-cell protection.** A, immunofluorescence images of the pancreatic tissue sections (stained by insulin, followed by TUNEL staining). The scale bars represent 20 μm. B, quantitative analysis of TUNEL (+) cells. Data expressed mean ± SEM, \*\*\*\* $p < 0.001$  of control to STZ, \*\* $p < 0.01$  of STZ to PK2. C, immunofluorescence images of the pancreatic tissue sections (stained for insulin and Ki67). The scale bars represent 20 μm. D, quantitative analysis of Ki67 (+) cells. Data expressed mean ± SEM, \* $p < 0.05$  of STZ. E, luminescence was determined for TXNIP promoter-luciferase construct transfected in INS-1 cells on PK2 treatment. Data expressed mean ± SEM, \*\* $p < 0.01$  of control. F, TXNIP Western blot results of INS-1 cells treated with PK2 for 30 min and DMSO in control as the vehicle.

the effect of PK2 in modulating the expression of TXNIP. INS-1 cells transfected with luciferase reporter constructs driven by the proximal TXNIP promoter were treated with PK2 (50 μM) (Fig. 7E). Indeed, our results demonstrated that PK2 attenuates TXNIP promoter activity (Fig. 7E). Lastly, we measured the TXNIP protein expression profile by Western blot on INS-1 cells in the presence and absence of PK2. We observed that PK2 treatment downregulates TXNIP. Taken together, our data indicate that PK2 attenuates the transcriptional activity of TXNIP, as well as its protein level, and thereby protects mice from STZ-induced β-cell damage.

## Discussion

In both T1DM and T2DM, pancreatic β cells mass and function are compromised. A recent report has suggested that a 40% β-cell mass reduction in young adults is insufficient to maintain glucose homeostasis and induce hyperglycemia—the progressive demise of β-cells in the etiology of T1DM (19). Though in T2DM, insulin resistance is an important pathogenic factor, ultimately causing the failure of β-cells or deficit in “functional β-cell mass” (inadequate compensatory insulin secretory response) (20). A loss of β-cell viability contributes to the development of absolute or relative insulin deficiency, as



observed in T1DM and T2DM patients, respectively. Therefore, targeting  $\beta$ -cells to improve  $\beta$ -cell function and survival is of utmost importance to develop newer therapies for the management of diabetes.

This report tried to fulfill the critical need to develop a small molecule that can protect and restore functional  $\beta$ -cell mass to combat diabetes. For this, we have target GLP1R, which has the ability to preserve  $\beta$ -cells mass and function. In this report, a selected set of small molecules were analyzed based on lowest binding energy and altered hydrophobic interactions ( $\pi$ - $\pi$  stacking) with GLP1R ECD. We compared developed small molecule interactions and binding energy with the existing GLP1R small molecule agonist. Further, we studied the designed sets of small molecules (PK2, PK3, and PK4) *in vitro* to analyze receptor internalization (21). Internalization of GLP1R by PK2-PK4 possibly represents that hydrophobic interactions are the meaningful interaction that drives complex stability even in dynamic nature and can be considered and validated further to design a novel small molecule agonist of GLP1R (21).

Moreover, MD simulation of the GLP1R-PK2 complex also implies that H-bonds and hydrophobic interactions are the main contributors to the stability of the ligand-receptor complex. Next, we also determined PK2-increased cAMP secretion, PKA activity, and the CREB phosphorylation at Ser133 residue that represents agonistic behavior of PK2 on GLP1R. Moreover, PK2 increases insulin secretion in presence of high glucose *in vitro*.

To determine the distribution of molecule *in vivo*, we determined the pharmacokinetic profile of PK2 in BALB/c mice. PK2 was found to have prolonged plasma  $t_{1/2}$  and  $t_{max}$  than Ex-4, which suggested good bioavailability and a longer half-life (22). Further, we examined the effect of PK2 in an *in vivo* model of STZ-induced  $\beta$ -cell death. PK2 treatment protects and reverses the impact of STZ-induced increase in blood glucose and decrease in serum insulin levels. Additionally, PK2 also protects  $\beta$ -cell mass. The enhanced  $\beta$ -cell mass can result either from the replication or hypertrophy of exciting  $\beta$ -cells. This was determined by TUNEL and Ki67 staining. The high percentage of Ki67 and insulin-positive cells and decrease in TUNEL (+) cells in PK2-treated mice suggested increased  $\beta$ -cell mass mainly resulting from augmentation of  $\beta$ -cell proliferation and decreased apoptosis. This increased  $\beta$ -cell mass also is correlated with increased basal insulin content and normal fasting plasma glucose level.

Treatment with STZ results in the production of superoxide radicals (23). TXNIP is a cellular redox sensor that increases in the presence of high glucose in diabetes. Next, we measured the effect of PK2 on the expression of TXNIP. Interestingly, we found that *in vitro* treatment of PK2 significantly inhibits the expression of TXNIP. Based on our *in vitro* data in cells and *in vivo* data in multiple low doses of STZ-treated mouse model, PK2 could mimic the protective effects by preventing and even reversing  $\beta$ -cell loss. Taken together, protections of  $\beta$ -cell functional mass by PK2 *in vivo* was attributable to increased  $\beta$ -cell proliferation and decreased  $\beta$ -cell apoptosis. Overall, this report presented a new strategy and a small

molecule GLP1R agonist, PK2, designed to rescue and protect  $\beta$ -cells from apoptosis and induce  $\beta$ -cell proliferation. We provide a structural features information platform for ligand (PK)-receptor (GLP1R) complexes which possibly be conducive to developing new GLP1R agonists in the future. We anticipate that the PK2 (orally active, nonpeptide GLP1R agonist) can help maintain functional  $\beta$ -cell mass, which is essential in preventing the development of T1DM and T2DM.

In summary, we designed and synthesized a series of small molecule GLP1R agonists. PK2, the model compound of the series, was used for pharmacologic potency, safety, and biological evaluation. Orally active PK2 demonstrates a balanced *in vitro* signaling profile that protects and restores functional  $\beta$ -cell mass, which is essential in preventing the development of T1DM and T2DM.

## Experimental procedures

### Screening of molecule

Autodock 4.2.6 and AutoDock tools 1.5.6 (24) were used to screen small molecule agonists of GLP1R. 3D structures of all the compounds with energy minimization were acquired through the BIOVIA DSV tool (BIOVIA DSV). Gasteiger charges for the screening were obtained by using BIOVIA DSV. Protein and ligand preparations and molecular docking parameters were performed comparably according to our past report and contrasted with the small molecule GLP1R agonists (11). The docked conformations of each compound were ranked into clusters based on their binding energy, and the best conformations were visually analyzed. Nonbonded interactions, including hydrogen bond, van der Waals,  $\pi$ - $\pi$ , and other electrostatic interaction between docked ligand and GLP1R were analyzed using BIOVIA DSV (25).

### Synthesis details of selected compounds

#### Preparation of 6,10b-dihydro-5aH-indolo[2,3-b]quinoxaline

A mixture of isatin (250 mg, 1.7 mmol) and ortho-phenylenediamine (183.5 mg, 1.7 mmol) in 500  $\mu$ l glacial acetic acid was heated at 120  $^{\circ}$ C and 25 W in a sealed vial for 10 min using a microwave reactor. The reaction mixture was poured in crushed ice; the precipitates were filtered and washed with ice-cold water thrice. Further, the dried yellow solid was triturated with a mixture of dichloromethane: methanol to get the pure product. Yellow solid,  $^1$ H NMR (1) (DMSO- $d_6$ , 500 MHz,  $\delta$ ): 12.05 (br s, -NH, 1H), 8.35 to 8.34 (d, J = 7.55 Hz, 1H), 8.26 to 8.24 (d, J = 8.25 Hz, 1H), 8.07 to 8.05 (d, J = 8.25 Hz, 1H), 7.80 to 7.77 (m, 1H), 7.72 to 7.68 (m, 2H), 7.59 to 7.57 (d, J = 8.25 Hz, 1H), and 7.37 to 7.34 (t, J = 7.55 Hz, 1H) ppm.  $^{13}$ C NMR (125 MHz, DMSO- $d_6$ ,  $\delta$ ): 145.83, 143.99, 140.14, 139.78, 138.58, 131.29, 129.04, 128.71, 127.47, 125.93, 122.24, 120.68, 118.97, 111.98 ppm. LRMS (ESI): calculated mass for  $C_{14}H_9N_3$  [M-H] $^+$ : 218.0718; found: 218.0739

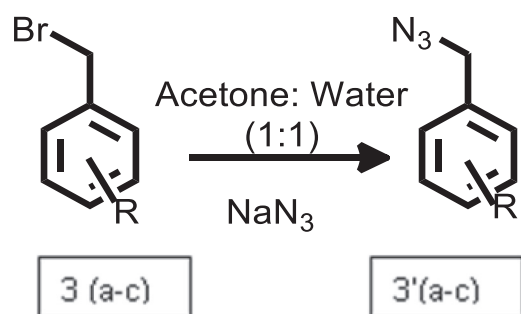
#### Preparation of 6-(prop-2-yn-1-yl)-6H-indolo[2,3-b]quinoxaline

To the mixture of compound 1 (1eq), anhydrous potassium carbonate (2 eq) in dry acetone (10 ml), propargyl bromide (1.5

## Small molecule agonist of glucagon-like-peptide-1 receptor

eq) was added, and the reaction mixture was refluxed for 4 h. The completion of the reaction was monitored using TLC. After the completion of the reaction, the solvent was removed under reduced pressure, and the crude was dissolved in ethyl acetate. The organic layer was washed with water twice, dried over anhydrous  $\text{Na}_2\text{SO}_4$ , and concentrated on rotavapor to get the orange-yellowish solid. This solid was triturated with hexane thrice to get the pure compound. Yellow solid,  $^1\text{H}$  NMR (2) ( $\text{CDCl}_3$ , 500 MHz,  $\delta$ ): 8.49 to 8.48 (d,  $J = 7.55$  Hz, 1H), 8.31 to 8.29 (dd,  $J_1 = 1.4$  Hz,  $J_2 = 8.25$  Hz, 1H), 8.15 to 8.13 (dd,  $J_1 = 1.35$  Hz,  $J_2 = 8.25$  Hz, 1H), 7.78 to 7.68 (m, 3H), 7.66 to 7.64 (d,  $J = 8.25$  Hz, 1H), 7.45 to 7.42 (t,  $J = 7.55$  Hz, 1H), 5.30 to 5.29 (d,  $J = 2.75$  Hz, 2H), 2.31 to 2.30 (m, 1H) ppm.  $^{13}\text{C}$  NMR (125 MHz,  $\text{CDCl}_3$ ,  $\delta$ ): 144.80, 143.48, 140.36, 140.11, 139.56, 131.06, 129.34, 128.95, 127.77, 126.32, 122.73, 121.56, 119.84, 110.13, 72.64, 30.56 ppm. LRMS (ESI): calculated mass for  $\text{C}_{17}\text{H}_{11}\text{N}_3$   $[\text{M}-\text{H}]^-$  256.0875; found: 256.2342

### Preparation of azido-benzene



Benzyl bromide (1 eq) was dissolved in a 1:1 acetone: water mixture, and sodium azide (2 eq) was added to this solution. The reaction was carried out in an open vessel at 65 °C (10 W) for 20 min. After completing the reaction, acetone was removed under reduced pressure, and the product was extracted using ethyl acetate. The organic layer was dried over sodium sulfate, and the solvent was removed on rotavapor. The azide formation was confirmed by FTIR, and it was directly used for the next step.

### Preparation of (PK2-PK4)

To a mixture of 9-substituted-6-propargyl-indolo [2,3-b] quinoxalines (1 eq) and (3'a-c) (1.5 eq) in dry THF, a freshly prepared solution of  $\text{CuSO}_4 \cdot 5\text{H}_2\text{O}$  (5 mol%) and sodium ascorbate (15 mol%) in water was added. The reaction was stirred at room temperature overnight. The progress of the reaction was monitored using TLC. After completing the reaction, the reaction mixture was filtered using Whatman filter paper, and the residue was dried using a rotary evaporator. Compound 6-((1-(4-nitrobenzyl)-1H-1,2,3-triazol-4-yl)methyl)-6H-indolo[2,3-b]quinoxaline (PK2), 6-((1-(4-methylbenzyl)-1H-1,2,3-triazol-4-yl)methyl)-6H-indolo[2,3-b]quinoxaline (PK3), and 6-((1-(4-methoxybenzyl)-1H-1,2,3-triazol-4-yl)methyl)-6H-indolo[2,3-b]quinoxaline (PK4) were

further purified using column chromatography. Characterization of synthesized compounds was performed using  $^1\text{H}$ -NMR,  $^{13}\text{C}$ -NMR, and mass spectrometry (Figs. S6–S10).

### Characterization data of (PK2-PK4)

#### PK2

Yellow solid, M. P. = 232 °C;  $^1\text{H}$  NMR ( $\text{CDCl}_3$ , 500 MHz,  $\delta$ ): 8.45 to 8.44 (d,  $J = 7.55$  Hz, 1H), 8.30 to 8.29 (d,  $J = 7.55$  Hz, 1H), 8.15 to 8.09 (m, 3H), 7.78 to 7.75 (m, 1H), 7.72 to 7.67 (m, 3H), 7.48 (s, 1H), 7.41 to 7.38 (m, 1H), 7.32 to 7.26 (m, 2H), 5.82 (s, 2H), 5.52 (s, 2H) ppm.  $^{13}\text{C}$  NMR (125 MHz,  $\text{CDCl}_3$ ,  $\delta$ ): 147.99, 145.10, 144.47, 143.79, 141.21, 140.34, 140.15, 139.48, 131.28, 129.39, 128.95, 128.54, 127.63, 126.31, 124.26, 122.72, 122.65, 121.49, 119.52, 110.26, 53.12, 36.77 ppm. LRMS (ESI): calculated mass for  $\text{C}_{24}\text{H}_{17}\text{N}_7\text{O}_2$   $[\text{M} + \text{H}]^+$ : 436.1522; found: 436.1545

#### PK3

Yellow solid, M. P. = 216 °C;  $^1\text{H}$  NMR ( $\text{CDCl}_3$ , 500 MHz,  $\delta$ ): 8.44 to 8.43 (d,  $J = 7.55$  Hz, 1H), 8.30 to 8.29 (d,  $J = 8.25$  Hz, 1H), 8.11 to 8.10 (d,  $J = 8.25$  Hz, 1H), 7.77 to 7.74 (m, 1H), 7.72 to 7.65 (m, 3H), 7.39 to 7.36 (m, 2H), 7.10 to 7.06 (m, 4H), 5.78 (s, 2H), 5.36 (s, 2H), 2.29 (s, 3H) ppm.  $^{13}\text{C}$  NMR (125 MHz,  $\text{CDCl}_3$ ,  $\delta$ ): 155.83, 145.12, 143.91, 143.80, 140.38, 140.16, 139.42, 138.66, 131.22, 129.70, 129.33, 128.81, 128.02, 127.70, 126.15, 122.54, 122.27, 121.33, 119.45, 110.46, 53.99, 36.85, 21.10 ppm. HRMS (ESI): calculated mass for  $\text{C}_{25}\text{H}_{20}\text{N}_6$   $[\text{M} + \text{H}]^+$ : 405.1822; found: 405.1819

#### PK4

Yellow solid, M. P. = 192.4 to 195 °C;  $^1\text{H}$  NMR ( $\text{CDCl}_3$ , 500 MHz,  $\delta$ ): 8.45 to 8.43 (d,  $J = 7.55$  Hz, 1H), 8.30 to 8.29 (d,  $J = 8.2$  Hz, 1H), 8.11 to 8.10 (d,  $J = 8.25$  Hz, 1H), 7.77 to 7.65 (m, 4H), 7.42 to 7.36 (m, 2H), 7.22 to 7.18 (t,  $J = 8.25$  Hz, 1H), 6.82 to 6.80 (m, 1H), 6.75 to 6.74 (d,  $J = 7.55$  Hz, 1H), 6.66 (s, 1H), 5.79 (s, 2H), 5.38 (s, 2H), 3.68 (s, 3H) ppm.  $^{13}\text{C}$  NMR (125 MHz,  $\text{CDCl}_3$ ,  $\delta$ ): 159.95, 145.11, 143.88, 140.37, 140.14, 139.42, 135.70, 131.22, 130.11, 129.33, 128.84, 127.69, 126.18, 122.56, 122.45, 121.35, 120.10, 119.46, 114.22, 113.40, 110.42, 55.18, 54.11, 36.84 ppm. LRMS (ESI): calculated mass for  $\text{C}_{25}\text{H}_{20}\text{N}_6\text{O}$   $[\text{M} + \text{H}]^+$ : 421.1771; found: 421.1798

### MD simulations

Long-term MD simulations were conducted to gauge the stability and conformational flexibility of GLP1R complex using GROMACS version 2018.4 (26) using Amber99SB-ILDN and General Amber force fields in the TIP3P water model. The system was electro-neutralized with 0.15 M NaCl. The electro-neutralized system was then subjected to energy minimization using a conjugate gradient algorithm on a converge threshold of 1 Kcalmol<sup>-1</sup> Å. The energy minimized system was subjected to equilibration through NVT and NPT ensemble for 1 ns each using the Leap-Frog algorithm. Finally, three seeded production run of 100 ns was conducted with an integration step of 0.002 fs at constant pressure (Parrinello–Rahman method) and

temperature (V-rescale method). LINCS and particle-mesh Ewald (PME) algorithms were used to constrain all hydrogen-bonds (H-bonds) and approximate long-range ionic-ionic interactions. The MD trajectory snapshots stored at every 20 ps were used for postdynamic analysis using GROMACS analysis toolkits. The intrinsic dynamics stability and flexibility parameters, including backbone RMSDs, C $\alpha$ -RMSFs, the radius of gyration ( $R_g$ ), and intermolecular hydrogen bond (H-bond) distribution were computed through *gmxrms*, *gmxrmsf*, *gmxgyrate*, and *gmxhbond* tools of GROMACS. The secondary structural elements in the protein-ligand complexes from each trajectory were analyzed using VMD. Protein-ligand interactions were analyzed using BIOVIA DSV, and Xmgrace was used to plot the 2-Dimensional graphs (Grace 5.1.21; <http://plasma-gate.weizmann.ac.il/Grace/>).

Principal component analysis was performed for the main-chain atoms of protein using built-in modules of GROMACS, that is, *gmxcovar* and *gmxcnvar*. The *gmxcluster* module was used for cluster analysis using the RMSD-based conformational clustering algorithm developed by Daura et al. (27) with a cut-off of 0.2 nm. The method tries to extract the maximally occupied clusters by taking into account the protein conformation with the lowermost RMSD to the centroid. To understand the decisive factor that drives the agonist (PK2) interaction with the GLP1R receptor, the MM/PBSA method was employed to compute the binding-free energy of the complex. In this study, *g\_mmpbsa* tool (compatible with GROMACS), which employs the MM/PBSA approach (28) was used to determine binding-free energy. A set of 1000 snapshot structures was extracted from the last 50 ns trajectories (50–100 ns) at an equal time interval for binding free energy estimation.

## Animals

Animal experiments were conducted following animal care and used committee-approved protocol at the Indian Institute of Technology Mandi. Mice were housed and maintained under a 12 h light/dark cycle at a temperature of 21 to 23 °C. Six- to seven-week-old BALB/c male mice were acclimated for 1 week before starting the experimental procedure. All animals were maintained on a control chow diet with free access to food and water. For GSIS, mice were starved for 6 h, PK2 was administered at the dose of 25 mg/kg body weight in the treated group, and the control group was administered with CMC-Na as a vehicle. After 1 h of treatment, glucose was injected with 2 mg/kg body weight, and blood was collected from the tail at 0, 10, 20, and 30 min from each mouse. Mice were divided into four groups wherein mice were subjected to different conditions: 1, vehicle group receiving 0.25% CMC and citrate buffer (Control); 2, the group received STZ alongside 0.25% CMC (STZ); 3, mice were infused with PK2 3 days before STZ injection (Pre-PK2), and 4, mice were injected with STZ, and PK2 was administered 1 day after STZ injection (Post-PK2). Low-dose (65 mg/kg) STZ in citrate buffer pH-4.0 injected IP for 5 days after overnight fasting, and PK2 (25 mg/kg) was administered orally over 18 days, and then mice were sacrificed. The complete scheme is described schematically in (Fig. 5A).

## GLP1R internalization

HepG2 cells were transfected with the hGLP1R-spark-GFP construct (Sino biologicals) using lipofectamine-3000 (Thermo Fisher Scientific). Transfected cells were treated with 20 nM of Exendin-4 (Ex-4) (positive control), PK2 (50  $\mu$ M), PK3 (50  $\mu$ M), and PK4 (50  $\mu$ M), and DMSO as a vehicle for 1 h. After completion of incubation, cells were washed with PBS and fixed using formalin. For antagonism of GLP1R receptor, 300 nM of Exendin (9–39) [Ex-9] was pretreated for 15 min followed by compound (PK2-50  $\mu$ M) treatment as described above. For cell surface labeling, cells were incubated with 1 mg/ml sulpho-NHS-biotin (Thermo Fisher Scientific) in PBS for 30 min at 4 °C, washed with PBS containing 100 mM glycine, and then fixed in 4% PFA for 15 min. Cells were blocked in 1% bovine serum albumin in PBS for another 30 min and then incubated in 5  $\mu$ g/ml of Texas-Red-avidin (Thermo Fisher Scientific) for 30 min. After extensive washing in PBS, the coverslips were mounted, and internalization of hGLP1R was observed using a Nikon Confocal Microscope.

## Insulin secretion assay

INS1 cells were used to measure insulin secretion, as previously mentioned (29). Briefly, INS1 cells were seeded in a 24-well plate. The following day, cells were transferred into a 5 mM glucose complete medium for the next 16 h, followed by the subsequent media change to 2.5 mM glucose for the next 1.5 h. Next, the cells were treated either with DMSO (as a vehicle) or with PK2 for 1.5 h at 16.7 mM glucose. The cell supernatant was then collected to measure insulin secretion. Insulin levels were measured using Rat Insulin ELISA Kit (Thermo) normalized with total protein content.

## PKA activity assay

293A cells were transfected with hGLP1R-spark-GFP constructs using lipofectamine-3000 after 48 h of transfection; cells were seeded at a density of  $1.0 \times 10^4$  cells/well in a 96-well plate. The next day, cells were treated with PK2 (50  $\mu$ M) and DMSO as a vehicle for 45 min in serum-free media. PKA activity was measured as per the manufacturer's protocol (Thermo Fisher Scientific#EIAPKA).

## cAMP assay

The intracellular cAMP levels were measured in 293A cells using a cAMP Glo assay kit (a luminescence-based assay) (Promega# V1501). Briefly, 293A cells were cultured in a 60 mm tissue culture-treated dish. Upon 70% confluency, the cells were transiently transfected with hGLP1R using lipofectamine 3000 following the manufacturer's protocol. After 4 h of transfection, the cells were seeded in a tissue culture grade 96-well plate at a density of  $5 \times 10^4$  cells/well and incubated overnight. The cells were treated with either DMSO (as vehicle) or different concentrations of PK2 (0.5, 10, 20, 100, 200, 300, 500, 1000, and 2000 nM) for 4 h. The media was aspirated, cells were lysed, and the cAMP levels were measured following the manufacturer's protocol. The EC<sub>50</sub> is calculated



## Small molecule agonist of glucagon-like-peptide-1 receptor

using GraphPad Prism5, and data are presented as relative luminescence.

### Western blot

Cells were lysed in RIPA lysis buffer containing protease and phosphatase inhibitors (Thermo Fisher Scientific), and the lysate was clarified by centrifugation at 15,000 rpm for 20 min at 4 °C. The protein concentration of the lysate was measured using a bicinchoninic acid protein assay (Thermo fisher scientific#23225). A sample buffer containing 2-mercaptoethanol was added to the total protein and heated at 95 °C for 5 min. The whole-cell lysate protein was resolved *via* (4–10%) SDS-PAGE unit and blotted onto polyvinylidene difluoride membranes (PVDF# BIO-RAD). Membranes were blocked in 5% bovine serum albumin or skimmed milk. Specific proteins were detected by incubation with appropriate primary and secondary (BIO-RAD) (horseradish peroxidase-conjugated) antibodies in TBST containing 5% bovine serum albumin. pCREB/CREB, pMAPK/MAPK, and  $\beta$ -actin were purchased from Cell Signaling Technology and TXNIP from Novus Biologicals. Antibodies used are provided in Table S3.

### Pharmacokinetics and tissue distribution of PK2 in-vivo

BALB/c male mice (5–6 weeks old, bodyweight  $25 \pm 2$  g) were administered PK2 orally at an equivalent dose of 25 mg/kg at different time points (0–24 h). Mice were sacrificed at different time points (5 min, 30 min, 1 h, 2 h, 4 h, 8 h, 16 h, and 24 h) after PK2 administration. Plasma, liver, heart, kidneys, lungs, spleen, and pancreas samples were harvested and stored at  $-80$  °C until analyzed. Concentrations of PK2 in plasma and tissue were examined using reverse-phase HPLC. Briefly, acetonitrile: methanol (1:1) is added into 100  $\mu$ l of plasma and homogenized tissue samples. The sample was sonicated and vortexed for 2 min, and debris was removed by centrifugation at 5000 rpm for 10 min. The organic layer was transferred to the fresh tubes and evaporated to dryness. The remaining residue was resuspended in 100  $\mu$ l of mobile phase, and 20  $\mu$ l resuspended aliquot injection was boosted into the HPLC column. Chromatographic separation was achieved using an Agilent reverse-phase C18-column ( $2.1 \times 50$  mm) at 28 °C. The mobile phase comprised of 0.1% trifluoroacetic acid in water/acetonitrile (40:60) was eluted at a 1 ml/min flow rate, and discharge was monitored at excitation of 350 nm and emission of 497 nm using a fluorescence detector. The amount of PK2 in the samples was quantified by measuring the peak area ratios of the PK2 using the standard curve. The pharmacokinetic parameters, including the area under the plasma concentration, half-life ( $T_{1/2}$ ), the apparent volume of distribution ( $V_d$ ), and systemic plasma clearance ( $C_L$ ) were determined by using standard methods.

### Immunohistochemistry

The tissues from each mouse were fixed in 4% PFA and embedded in paraffin for sectioning. Sections were deparaffinized using xylene, washed with ethanol, and rehydrated with decreasing ethanol percentage. Antigen retrieval

was performed using a citrate buffer of pH-6.0 after sections were incubated at 4 °C for another 1 h. Sections were washed using PBS and then permeabilized using 0.1% Triton X-100. The sections were blocked in 5% horse serum in PBS at room temperature for 1 h, followed by primary antibody overnight incubation with anti-insulin (1:200) and anti-Ki67 (1:100) (Abcam) in 5% horse serum at 4 °C. Sections were then washed with TBST three times for 5 min each and then were incubated with the Alexa fluor secondary antibody (Jackson Immuno Research) at dilution of 1:500 at room temperature for 3 h. DAPI was used for staining the nuclei. Microscopic images were then captured using a Zeiss microscope (40 $\times$  objective). The quantification was carried out with the ImageJ software. Antibodies used are provided in Table S3.

### TUNNEL assay

The double immunofluorescent staining of insulin and TUNEL were performed according to the standard procedures. In brief, the sections were incubated with primary antibody anti-insulin (1:200). Sections were then incubated with Alexa fluor-conjugated secondary antibody (Jackson Immuno Research) at 1:500 diluted in PBST at room temperature for 2 h in the dark. The sections were fixed using PFA for 15 min, and the TUNEL signal was stained according to the manufacturer's instructions (Promega). Microscopic images were then captured in a Zeiss microscope using a 40 $\times$  objective.

### TXNIP promoter activity assay

INS-1 cells were seeded in a 35 mm dish at a confluence of 60 to 70%. The next day, cells were transfected with TXNIP promoter-luciferase construct (Addgene) for 48 h. After the transfection, cells were trypsinized and seeded in 96-well white plate. Cells were given a treatment of 50  $\mu$ M-PK2 and DMSO as a vehicle in control for 45 min. After incubation, a steady Glo reagent (Promega) was added to each well and incubated for another 10 min. Luminescence was determined by using an iTECAN multi-plate reader.

### Quantification and statistical analysis

Data are presented as mean  $\pm$  SEM. The Student's unpaired *t* test was used to analyze significant differences between means using GraphPad Prism. Statistics are mentioned in the figure legends, and a *p*-value of  $\leq 0.05$  was considered statistically significant.

### Data availability

The datasets supporting the conclusions of this article are included within the article and its supporting information.

---

**Supporting information**—This article contains supporting information.

**Acknowledgments**—We sincerely thank the Advanced Materials Research Centre and BioX Centre of IIT Mandi for the research

facilities. We thank Prateep Singh Sagara and other members of the PM Lab for useful discussions.

**Author contributions**—P. M. conceptualization; K. G., P. G., B. D., S. K., S. G., and P. M. methodology; P. M. supervision; K. G., S. T., P. G., A. C., S. D., B. D., S. K., B. B., D. K. D., S. G., investigation; K. G. formal analysis; K. G., S. G., and P. M. writing—original draft; K. G., S. T., P. G., A. C., S. D., B. D., S. K., B. B., D. K. D., S. G., and P. M. writing—review and editing; K. G. validation; K. G. software; K. G. data curation; K. G. visualization; P. M. project administration; P. M. funding acquisition.

**Funding and additional information**—K. G. thanks the University Grant Commission (UGC), India, for the research fellowship. P. M. would like to acknowledge support from the Department of Biotechnology (DBT), Government of India (BT/PR27786/MED/30/1980/2018) for financial aid. This work was supported by Science and Engineering Board (SERB) Government of India, India (CRG/2019/004006) to P. M.

**Conflict of interest**—No potential conflicts of interest relevant to this article were reported.

**Abbreviations**—The abbreviations used are: CREB, cAMP response element-binding protein; DSV, discovery studio visualizer; ECD, ectodomain; GLP1R, Glucagon-like-peptide-1 receptor; MM/PBSA, the molecular mechanics-based Poisson–Boltzmann surface area; RMSE, root mean square fluctuations; T1DM, type 1 diabetes mellitus; T2DM, type 2 diabetes mellitus.

## References

- International Diabetes Federation (2021) *IDF Diabetes Atlas*, 10th Ed., International Diabetes Federation, Brussels
- Wang, M. W., Liu, Q., and Zhou, C.-h. (2010) Non-peptidic glucose-like peptide-1 receptor agonists: Aftermath of a serendipitous discovery. *Acta Pharmacol. Sin.* **31**, 1026–1030
- Fletcher, M. M., Halls, M. L., Christopoulos, A., Sexton, P. M., and Wooten, D. (2016) The complexity of signalling mediated by the glucagon-like peptide-1 receptor. *Biochem. Soc. Trans.* **44**, 582–588
- Widmann, C., Dolci, W., and Thorens, B. (1995) Agonist-induced internalization and recycling of the glucagon-like peptide-1 receptor in transfected fibroblasts and in insulinomas. *Biochem. J.* **310**, 203–214
- Samson, S. L., and Garber, A. (2013) GLP-1R agonist therapy for diabetes. *Curr. Opin. Endocrinol. Diabetes Obes.* **20**, 87–97
- Knudsen, L. B., Kiel, D., Teng, M., Behrens, C., Bhumralkar, D., Kodra, J. T., Holst, J. J., Jeppesen, C. B., Johnson, M. D., de Jong, J. C., Jorgensen, A. S., Kercher, T., Kostrowicki, J., Madsen, P., Olesen, P. H., *et al.* (2007) Small-molecule agonists for the glucagon-like peptide 1 receptor. *Proc. Natl. Acad. Sci. U. S. A.* **104**, 937–942
- Sloop, K. W., Willard, F. S., Brenner, M. B., Ficorilli, J., Valasek, K., Showalter, A. D., Farb, T. B., Cao, J. X. C., Cox, A. L., Michael, M. D., Gutierrez-Sanfeliciano, S. M., Tebbe, M. J., and Coghlan, M. J. (2010) Novel small molecule glucagon-like peptide-1 receptor agonist stimulates insulin secretion in rodents and from human islets. *Diabetes* **59**, 3099–3107
- Morris, L. C., Nance, K. D., Gentry, P. R., Days, E. L., Weaver, C. D., Niswender, C. M., Thompson, A. D., Jones, C. K., Locuson, C. W., Morrison, R. D., Daniels, J. S., Niswender, K. D., and Lindsley, C. W. (2014) Discovery of (S)-2-cyclopentyl-N-((1-isopropylpyrrolidin-2-yl)-9-methyl-1-oxo-2,9-dihydro-1H-pyrido[3,4-b]indole-4-carboxamide (VU0453379): A novel, CNS penetrant glucagon-like peptide 1 receptor (GLP1R) positive allosteric modulator (PAM). *J. Med. Chem.* **57**, 10192–10197
- Willard, F. S., Bueno, A. B., and Sloop, K. W. (2012) Small molecule drug discovery at the glucagon-like peptide-1 receptor. *Exp. Diabetes Res.* **2012**, 709893
- Yang, D., de Graaf, C., Yang, L., Song, G., Dai, A., Cai, X., Feng, Y., Reedtz-Runge, S., Hanson, M. A., Yang, H., Jiang, H., Stevens, R. C., and Wang, M.-W. (2016) Structural determinants of binding the seven-transmembrane domain of the glucagon-like peptide-1 receptor (GLP-1R). *J. Biol. Chem.* **291**, 12991–13004
- Girdhar, K., Dehury, B., Kumar Singh, M., Daniel, V. P., Choubey, A., Dogra, S., Kumar, S., and Mondal, P. (2018) Novel insights into the dynamics behavior of glucagon-like peptide-1 receptor with its small molecule agonists. *J. Biomol. Struct.* **37**, 3976–3986
- Underwood, C. R., Garibay, P., Knudsen, L. B., Hastrup, S., Peters, G. H., Rudolph, R., and Reedtz-Runge, S. (2010) Crystal structure of glucagon-like peptide-1 in complex with the extracellular domain of the glucagon-like peptide-1 receptor. *J. Biol. Chem.* **285**, 723–730
- Morris, G. M., Huey, R., and Olson, A. J. (2008) Using AutoDock for ligand-receptor docking. *Curr. Protoc. Bioinform.* **24**. <https://doi.org/10.1002/0471250953.bi0814s24>
- Thompson, A., and Kanamarlapudi, V. (2015) Agonist-induced internalisation of the glucagon-like peptide-1 receptor is mediated by the Gαq pathway. *Biochem. Pharmacol.* **93**, 72–84
- Eason, C. T., Bonner, F. W., and Parke, D. V. (1990) The importance of pharmacokinetic and receptor studies in drug safety evaluation. *Regul. Toxicol. Pharmacol.* **11**, 288–307
- Wang, R. N., Bouwens, L., and Kloppel, G. (1994) Beta-cell proliferation in normal and streptozotocin-treated newborn rats: Site, dynamics and capacity. *Diabetologia* **37**, 1088–1096
- Chen, J., Saxena, G., Mungrue, I. N., Lusis, A. J., and Shalev, A. (2008) Thioredoxin-interacting protein A critical link between glucose toxicity and β-cell apoptosis. *Diabetes* **57**, 938–944
- Masson, E., Koren, S., Razik, F., Goldberg, H., Kwan, E. P., Sheu, L., Gaisano, H. Y., and Fantus, I. G. (2009) High β-cell mass prevents streptozotocin-induced diabetes in thioredoxin-interacting protein-deficient mice. *Am. J. Physiol. Metab.* **296**, E1251–E1261
- Klinke, D. J. (2008) Extent of beta cell destruction is important but insufficient to predict the onset of type 1 diabetes mellitus. *PLoS One* **3**, e1374
- Cnop, M., Welsh, N., Jonas, J.-C., Jöns, A., Lenzen, S., and Eizirik, D. L. (2005) Mechanisms of pancreatic β-cell death in Type 1 and Type 2 Diabetes. *Diabetes* **54**, S97–S107
- Jones, B., Buenaventura, T., Kanda, N., Chabosseau, P., Owen, B. M., Scott, R., Goldin, R., Angkathunyakul, N., Corrêa Jr, I. R., Bosco, D., Johnson, P. R., Piemonti, L., Marchetti, P., Shapiro, A. M. J., Cochran, B. J., *et al.* (2018) Targeting GLP-1 receptor trafficking to improve agonist efficacy. *Nat. Commun.* **9**, 1602
- Liao, S., Liang, Y., Zhang, Z., Li, J., Wang, J., Wang, X., Dou, G., Zhang, Z., and Liu, K. (2015) *In vitro* metabolic stability of exendin-4: Pharmacokinetics and identification of cleavage products. *PLoS One* **10**, e0116805
- Szkudelski, T. The mechanism of alloxan and streptozotocin action in B cells of the rat pancreas. [researchgate.net](https://www.researchgate.net/publication/234411111).
- Morris, G., and Huey, R. (2009) AutoDock4 and AutoDockTools4: Automated docking with selective receptor flexibility. *J. Comput. Chem.* **30**, 2785–2791
- Khanderao, A., Sankunni, J., and Karuppaiyil, M. (2017) Molecular docking studies on thirteen fluoroquinolones with human topoisomerase II a and b. *In Silico Pharmacol.* **5**, 4
- Abraham, M. J., Murtola, T., Schulz, R., Páll, S., Smith, J. C., Hess, B., and Lindahl, E. (2015) Gromacs: High performance molecular simulations through multi-level parallelism from laptops to supercomputers. *SoftwareX* **1–2**, 19–25
- Daura, X., Gademann, K., Jaun, B., Seebach, D., van Gunsteren, W. F., and Mark, A. E. (1999) Peptide folding: When simulation meets experiment. *Angew. Chem. Int. Ed.* **38**, 236–240
- Wang, C., Greene, D. A., Xiao, L., Qi, R., and Luo, R. (2018) Recent developments and applications of the MMPBSA method. *Front. Mol. Biosci.* **4**, 87
- Daniel, P. V., Kamthan, M., Thakur, S., and Mondal, P. (2022) Molecular pathways dysregulated by Pb<sup>2+</sup> exposure prompts pancreatic beta-cell dysfunction. *Toxicol. Res.* **11**, 206–214